Phonon band gaps in the IV-VI monochalcogenides

Uri Argaman,[1] Ran E. Abutbul,[1,2] Yuval Golan,[1,2] and Guy Makov [1,2]

[1]*Materials Engineering Department, Ben-Gurion University of the Negev, Beer-Sheva 84105, Israel*
[2]*Ilse Katz Institute for Nanoscale Science and Technology, Ben-Gurion University of the Negev, Beer-Sheva 84105, Israel*

The origin of the phonon band gap and its controlling factors in low-symmetry crystals are studied in the monochalcogenide family of semiconductors through a combination of first-principles calculations and the introduction of quantitative measures of bond distortion in phonon modes. The phonon spectra were calculated for the recently discovered low-symmetry 64-atom cubic π-phase of the monochalcogenides in four materials: SnS, SnSe, GeS, and GeSe. The phonon spectra of all these systems exhibit phonon band gaps in the optical phonon spectrum with widths of 0.7–2 THz. Raman measurements were performed that support the existence and magnitude of the calculated phonon band gaps in π-SnS and π-SnSe. The origin of the phonon band gaps was examined through the contributions of the bond strengths and of the mass differences to the phonon spectrum in several monochalcogenide phases. An analysis of the normal modes found more rigid bond motion below the phonon gap and less rigid bond motion above the gaps as well as differences in the relative motion of the two types of atoms. These differences are identified as originating from the acoustic and optical modes of the symmetric parent rocksalt structure. The effect of the phonon band gap on the thermodynamic properties is discussed.

I. INTRODUCTION

Band gaps in the phonon spectrum, representing a range of forbidden frequencies, are well-known in several classes of systems, including molecular crystals (e.g., Ref. [1]) and systems with rigid units [2–6]. In high-symmetry structures of binary compounds, a phonon band gap between the acoustic and optical modes, familiar from elementary textbook one-dimensional systems, may appear and is typically assigned to the mass difference between the atoms forming the binary compound [7–9].

Another possible explanation for a phonon band gap is differences in the rigidity (of deformation) of the modes. In several studies, the concept of rigid-unit modes (RUMs) was introduced [2–6]. The RUMs are phonon modes in which groups of atoms move together as a rigid unit and thus do not distort the bonds connecting the atoms within the unit. Because of the rigidity of the motion, these normal modes typically have low frequencies. The RUMs have been used to explain displacive phase transitions [4–6] and negative thermal expansion [2,3].

Recently, phonon band gaps in binary compound semiconducting systems have been shown to play a significant role in determining the thermal conductivity of these materials in both three-dimensional (3D) [10,11] and two-dimensional (2D) [12,13] structures leading to the experimental discovery of high thermal conductivity in boron arsenide (BAs) [14]. Furthermore, studies of nanometric systems have uncovered the previously unappreciated role of optical phonons in affecting thermal transport [15] by scattering acoustic phonons [16]. Indeed, Gu *et al.* [12] found that the phonon band gap increases the thermal conductivity in two-dimensional MoS_2 and WS_2 by making some scattering processes inefficient.

They suggested that the existence of the phonon band gap in these materials is due to the mass difference between the component atoms.

These developments indicate the possible utility of phonon band-gap engineering to control thermal conductivity through material design. Controlling the thermal conductivity should prove useful in designing novel and improved thermoelectric materials. However, achieving this goal will require a better understanding of the origin of phonon band gaps and the factors controlling them.

Band gaps are of course well known in the spectrum of the electronic states of crystals. An opening of an electronic band gap can be explained as the result of a structural distortion, e.g., in one dimension the Peierls distortion [17] and its three-dimensional manifestation in several semiconductors and semimetals [17–20]. The electronic band gap also has a significant effect on thermal and transport properties of electrons in materials [21]. This suggests an analogy for the origin of the phonon band gap in the optical spectrum due to symmetry breaking and its possible significance in the thermal and transport properties of phonons in crystals.

The IV-VI monochalcogenides have been the focus of extensive research attention in recent years due to their extensive potential applications, e.g., in thermoelectric devices, solar cells, and near-infrared detectors [22–25]. These materials form a variety of crystalline structures, the properties of which are strongly affected by the lone-pair electrons on the group-IV atoms, which makes them also of fundamental interest [26–28]. In particular, the IV-VI monochalcogenides have electronic band gaps ranging from 0 to 2 eV, which can be either direct or indirect, and are strongly dependent on the crystallographic phase.
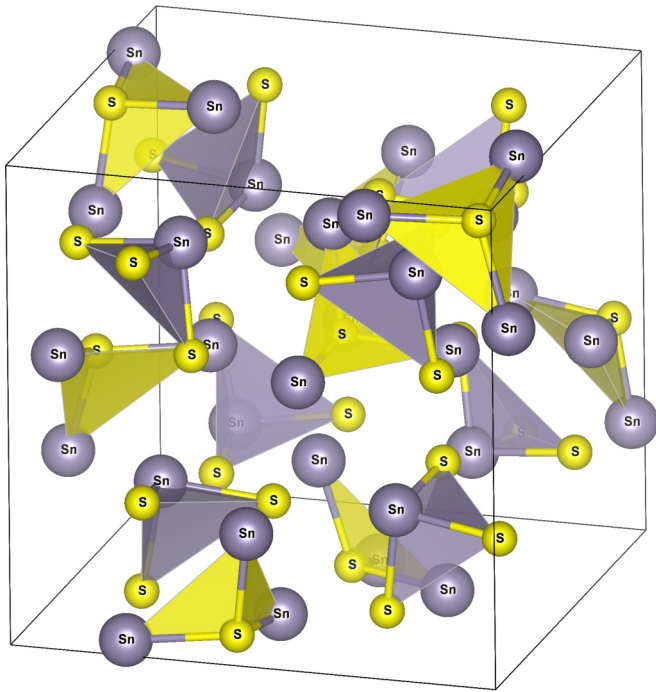
FIG. 1. The primitive unit cell of the π structure (in SnS).

The IV-VI monochalcogenides are formed in several different phases. The rocksalt phase has the highest symmetry and is stable at high temperature or at high pressure as well as at zero pressure and zero Kelvin in the lead chalcogenides [29]. The rhombohedral phase is a distortion of the two-atom primitive unit-cell rocksalt structure. This phase is stable in GeTe and SnTe and also mechanically stable at zero pressure and 0 K in GeSe and SnSe [28]. As the pressure is increased this phase approaches the high-symmetry rocksalt phase, and at negative pressures it deviates more strongly from the rocksalt phase. With even lower symmetry, the orthorhombic phase has eight atoms per primitive unit cell and is the stable phase at ambient conditions in tin and germanium monochalcogenides. These last two phases are layered structures in which stronger bonds form between the atoms inside the layer and weaker bonds connect neighboring layers.

Recently, a previously unknown cubic phase with a large, low-symmetry 64-atom unit cell was synthesized in the binary systems SnS and SnSe [24,30,31], denoted as π-phase. The π-phase structure is shown in Fig. 1, illustrating that it is not a layered structure like other monochalcogenide phases. This phase has since attracted extensive interest in the materials community due to its unusual properties and potential for applications [23,24,30–34]. The formation energies of this new phase were determined by density-functional theory (DFT) calculations [26,27] and shown to be energetically competitive with the stable orthorhombic phases for SnS and SnSe. This was also found to be the case for GeS and GeSe, which have yet to be synthesized. The stability of the π-phase in SnS was confirmed by phonon calculations that showed it to be mechanically stable [27,35]. More surprisingly, these calculations also found that this new phase exhibits a large phonon band gap in the optical band, and they suggested that this band gap originates in the mass difference between Sn

and S. However, other members of this family show smaller or even nonexisting band gaps, whereas other materials with larger mass differences such as the lead monochalcogenides do not exhibit band gaps [29]. Furthermore, the π-phase does not exhibit typical RUM low-frequency modes. Therefore, it may be assumed that there exist additional factors that determine the formation of the phonon band gaps.

The phonon spectrum has also been calculated for other phases of the IV-VI monochalcogenides. The stable orthorhombic *Pnma* phase exhibits a small phonon band gap [36], while the rhombohedral phase does not show a band gap at zero pressure. Under a tension of -2 GPa, a phonon band gap opens between the acoustic and optical branches of the spectrum, together with an increased distortion of the crystal structure [28]. Finally, the high-symmetry rocksalt phase is not mechanically stable for germanium or tin monochalcogenides at zero pressure and 0 K but at higher pressures it is stabilized and a phonon band gap does not appear [36].

Thus the monochalcogenides present an opportunity to study the factors controlling the formation of phonon band gaps within a single material system and the effect of such band gaps on the thermophysical properties of materials. The objective of the present study is to explore structural distortion as a mechanism for the formation of phonon band gaps in binary crystalline systems using the IV-VI monochalcogenides as a model system. Despite the development of multiple tools to calculate phonon frequencies and modes in recent years [37–39], many analyses, even for complex systems such as the π-phase with its 192 Γ-point phonon modes, rely on symmetry classifications and visual representation of the phonon modes [27,35], which restricts the analysis. Therefore, we begin this study by introducing several analytical quantities to characterize quantitatively the deformation of bonds and phonon modes. Subsequently, we calculate the phonon spectrum of the π-phase of the IV-VI monochalcogenides from first principles and investigate their phase stability, in particular for GeS and GeSe, which have not yet been obtained experimentally. We also measure the Raman spectrum to examine the phonon spectra and obtain good agreement with the calculations confirming their validity. We find that all these systems exhibit large phonon band gaps in the optical band, thus indicating that mass differences are not the sole origin of this phenomenon. We explore the effect of distortion of the crystal structure from the high-symmetry rocksalt phase on the phonon spectrum. In particular, the properties of the normal modes on both sides of the phonon band gap are studied and are shown to be related to the acoustic and optical phonons of the undistorted structure. Finally, we consider the effect of the phonon band gap on the thermodynamic properties.

II. METHODS

A. Experimental details

1. Materials

Tin(II) chloride (SnCl$_2$, reagent grade, 98%), oleylamine (OLA, >98%), thiourea (reagent grade, 98%), selenourea (98%), and oleic acid (technical grade, 90%) were purchased from Sigma-Aldrich and used without further purification.

Hydrochloric acid (32% w/w), sulfuric acid (95%), methanol (99.8%), and chloroform (99.9%) were purchased from Bio-Lab and used without further purification.

2. Oleyammonium chloride (OACL) synthesis

The preparation consisted of titrating hydrochloric acid over sulfuric acid while the evolved gas was dihydrated and transferred to OLA. This process was stopped when the bubbles evolved from the OLA, indicating a full reaction with HCl.

3. SnS synthesis

56.8 mg of $SnCl_2$, 4 mL of OLA, and 1.5 mL of oleic acid were placed in a three-necked flask inside a glove-box. 22 mg of thiourea and 3 mL of OLA were placed in another three-necked flask inside a glove-box. Both flasks were fitted with a condenser and a thermometer and connected to a Schlenk line. Reactions occurred under a nitrogen inert atmosphere. The Sn precursor was heated to $180\,°C$ for 1 h until $SnCl_2$ completely dissolved. Meanwhile, the S precursor was heated to $170\,°C$ for 1 h. The S precursor was injected into the Sn precursor and the reaction occurred, indicated by an instantaneous color change to brown. The incubation time was set to 5 min.

4. SnSe synthesis

56.8 mg of $SnCl_2$, 4.25 mL of OLA, 0.5 mL of oleic acid, and 760 mg of OACl were placed in a three-necked flask in a glove-box and transferred to the Schlenk line. The flask was fitted with a condenser and a thermometer. 18 mg of selenourea and 1.5 mL of OLA were placed in an amber vial inside a glove-box and transferred to a bench-top sonicator. Sonication time was set to 30 min until the selenourea fully dissolved. Both reactions occurred under a nitrogen inert atmosphere. The Sn precursor was heated to $130\,°C$ for 1 h until $SnCl_2$ completely dissolved. The Se precursor was injected to the Sn precursor and the reaction occurred, indicated by an instantaneous color change to deep brown. The incubation time was set to 5 min.

5. Cleaning procedures

The nanoparticles were quenched to room temperature by injecting methanol into the hot reaction flask after removing the heating mantle. The solution was transferred to a 50 mL test tube and centrifuged at 2500 rpm for 5 min. Particles were redispersed with 5 mL of chloroform and precipitated again using 45 mL of methanol. The particles were centrifuged again and this cleaning procedure repeated twice.

6. Raman

The Raman system was comprised of the LabRAM HR Evolution (HORIBA, France) micro-Raman system. The excitation source was an argon laser (532 nm) with a power of 3 mW on the sample. In most of the measurements, the laser power was reduced by 40 using filters. The laser was focused with a $100\times$ objective to a spot of about 4 μm in diameter. The grating used was 1800 gmm^{-1} with a confocal hole of 100 μm. Samples were cooled to liquid nitrogen temperature using a cold stage.

B. Computational details

The electronic structure and the total energies were calculated using a norm-conserving pseudopotential plane-waves method [40]. Phonon spectra were calculated using density functional perturbation theory [37]. All calculations were performed with the QUANTUM ESPRESSO package [41]. The exchange-correlation functional was approximated with the PBE general gradient approximation (GGA) [42], which was previously found to be in good agreement with experiment for these systems [26,43]. Pseudopotentials were obtained from the PSlibrary of QUANTUM ESPRESSO and a kinetic energy cutoff of 70 Ry was used in all calculations. The k-point mesh employed was $2 \times 2 \times 2$, which yields a convergence of 0.02 THz in the phonon frequencies of the π-phase systems.

C. Characterization of the phonon polarization

Phonon polarization describes the relative motions of the atoms in the unit cell within a phonon mode. Both mass differences and the crystal bonding affect the polarization of phonons. In the following sections, we shall study both of these effects and characterize the motion of the atoms in normal modes of binary systems. We introduce three dimensionless quantities: The relative motion ratio (RMR), the bond deformation parameter (BDP), and the mode deformation parameter (MDP). The RMR is defined as

$$\text{RMR} = \frac{\sum_i \left| \vec{P}_i^X \right|}{\sum_j \left| \vec{P}_j^M \right|}, \tag{1}$$

where $\vec{P}_i^X$ is the polarization of the ith atom of species X, where X is a chalcogenide and M is a metal of column IV, in a particular normal mode, and the sum is over all the atoms of type X in the unit cell. This parameter measures the relative contribution of the atomic motions of each of the two constituent elements in these compounds to the total motion in the mode. The RMR can take on values ranging from 0, corresponding to no motion of the chalcogenide atoms, through 1, corresponding to equal aggregate motions of both types of atoms, up to infinity corresponding to static metal atoms with only the chalcogenide atoms moving.

The BDP is defined for any bond between atoms i and j of species X and Y with polarizations $\vec{P}_i^X$ and $\vec{P}_j^Y$, respectively (see Fig. 2), as

$$\Delta_{ij} = \frac{\left| \left(\vec{P}_i^X - \vec{P}_j^Y \right) \cdot \hat{r}_{ij} \right|}{\left| \vec{P}_i^X \cdot \hat{r}_{ij} \right| + \left| \vec{P}_j^Y \cdot \hat{r}_{ij} \right|}, \tag{2}$$

where $\hat{r}_{ij}$ is a unit vector in the bond direction (between atoms i and j). This definition is based on the definition of the strain in the direction of the bond and is zero for rigid translations and rotations, as shown in Appendix A. Values of the BDP can range between 0 and 1 corresponding to complete absence of or pure compression/extension of the bond, respectively, as illustrated in Fig. 2. The BDP does not depend on the norm of the eigenvector of the dynamical matrix (if the polarization of all the atoms will be multiplied by a constant it will not change the BDP) and thus it does not depend on the phonon occupation or temperature.
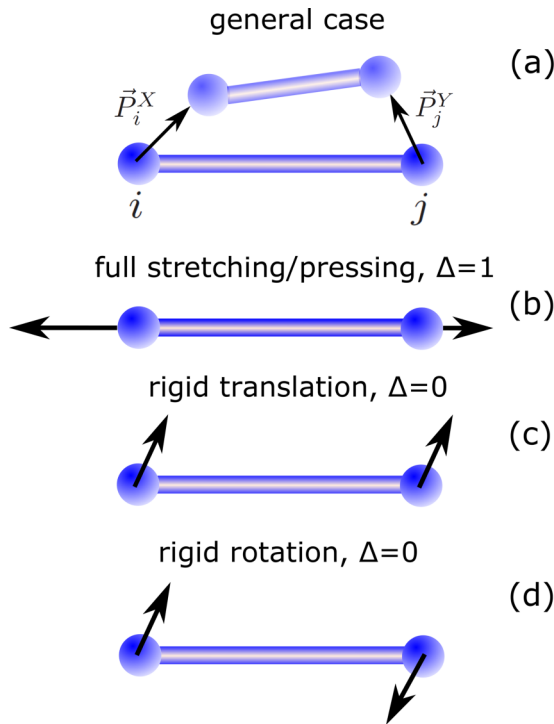
FIG. 2. Schematic illustration of the BDP in the general case of polarization and in some limiting cases. The circles represent the atoms, the rods represent the bond, and the solid arrows represent the polarization.

FIG. 3. Schematic illustration of the (a) frequency and (b) MDP for a diatomic chain with two spring constants: $c_1 = 2c_2$.

Phonon excitations always involve multiple bonds, and therefore we introduce a mode deformation parameter (MDP), which is an average of the BDP over the nearest-neighbor bonds and all the atoms in the unit cell and is defined by

$$\Lambda = \frac{2}{N_{UC}N_{NN}} \sum_{i,j} \Delta_{ij}, \qquad (3)$$

where N_{UC} is the number of atoms in the unit cell and N_{NN} is the number of first nearest neighbors. In the present systems, N_{NN} is equal to 3. The sum is over all nonequivalent pairs of first nearest neighbors of the atoms (the 2 factor is for double counting in $N_{UC}N_{NN}$). The MDP values also range between 0 and 1, where 1 is a normal mode with all bonds in the unit cell compressed or stretched, and 0 is a fully rigid normal mode.

The physical significance of these definitions can be clarified further by considering simple analytical models of linear chains of atoms. In these models, different masses of the atoms create two types of branches, commonly denoted as acoustic and optic, with different RMR, which increases as the mass ratio is increased. For example, in the linear chain with two atoms in the unit cell with masses M_1 and M_2, the RMR in the optical branch at the Γ point is M_2/M_1 and for the acoustic branch it is 1. Furthermore, different bond strengths (commonly represented as springs) can also create two types of branches with different MDP. The MDP of all modes in a linear chain with a single atomic mass and two different alternating spring constants is shown in Fig. 3. The MDP, Λ, takes on values close to 1 for the optical branch and well below 0.5 for the acoustic branch. Intermediate values of
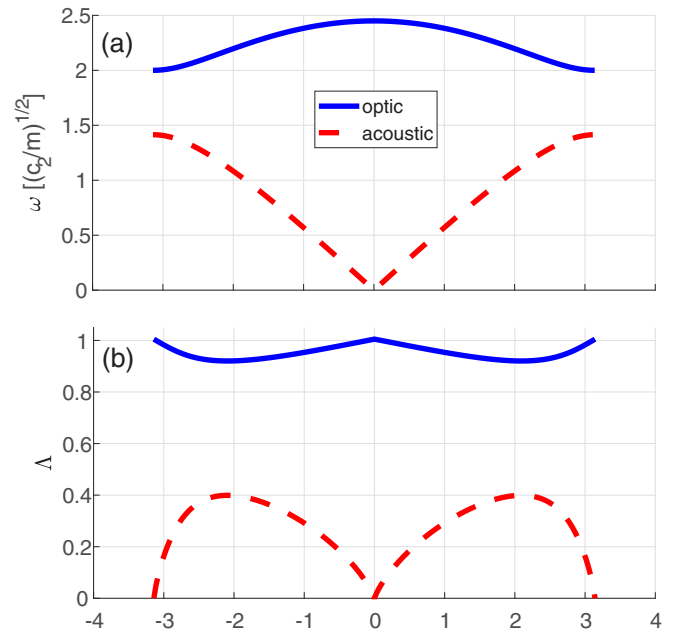
the MDP between the values for the acoustic branch and the optical branch are forbidden in this linear chain.

III. PHONON SPECTRUM RESULTS

A. π-phase phonon frequencies

Calculations of the phonon frequencies at the Γ-point were performed for the materials SnS, SnSe, GeS, and GeSe in the π-phase in the primitive 64-atom unit cell, and the results are presented in Fig. 4. All four materials are found to have only positive (real) frequencies, which indicate that they are all mechanically stable in the π-phase including GeS and GeSe, which have not yet been observed experimentally.

In the present study, to reduce computational costs, we assume that the phonon dispersion, particularly near the phonon band gap, is negligible with the exception of the three acoustic branches and that therefore the spectrum at the Γ-point is representative of the entire Brillouin zone. To confirm this assumption, we also calculated the phonon spectrum of SnS at the X point on the boundary of the Brillouin zone and saw no significant change in the band gap (Fig. 4). In addition, a calculation of the phonon spectrum at three q-points in the Brillouin zone of the π-phase of SnS by Skelton *et al.* [35] also agrees with this assumption.

In all four material systems studied, we found phonon band gaps at the Γ-point. Both the magnitude of the band gap and the frequency at which it occurs vary from one system to another. The largest gap is found in GeS and the smallest in SnSe. The mass differences are largest in SnS and smallest in GeSe. This indicates that there are additional effects beyond mass differences that contribute to the band gap. We note that the phonon band gaps in all these materials occur exactly in the middle of the phonon spectrum, which contains 96 normal modes below the gap (including the zero-frequency acoustic modes) and 96 above the gap. Similar results are found for
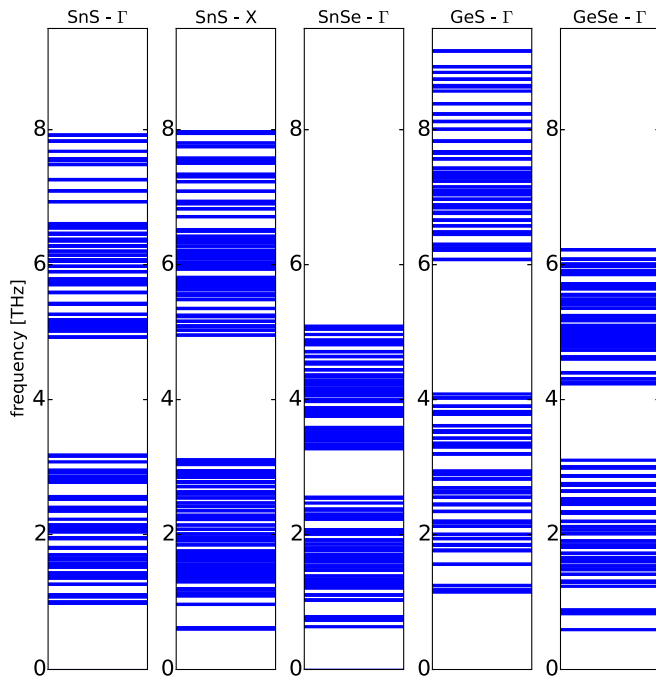
FIG. 4. The Γ-point phonon frequencies in the π-phase of SnS, SnSe, GeS, and GeSe. For SnS, the frequencies are shown also for the high-symmetry X point.

other monochalcogenide systems that exhibit a phonon band gap [36].

B. SnS π-phase phonon frequencies with the same masses for the Sn and S atoms

To obtain better insight into the phenomenon of the phonon band gap in the π-phase and to test the hypothesis that it originates in mass differences between the atoms [27], we recalculated the phonon frequencies of π-SnS assigning a fictitious mass to both atomic species equal to the average of the masses of Sn and S (Fig. 5). In this case with equal masses, the band gap is found to be approximately half the size of the band gap formed when the atoms are assigned their real masses. Furthermore, we find that this choice of the masses has almost no effect on the frequencies below the band gap. However, a significant effect is observed on the frequencies above the band gap, indicating a qualitative difference between the two sets of modes, which we explore below in Sec. IV.

C. π-phase phonon frequencies at high pressure

Relaxation of the crystal structure of π-SnS was performed under pressures up to 10 GPa, and the corresponding phonon spectra were calculated. It was found that the crystal retains its π-phase structure and all phonon modes are real, indicating continued mechanical stability. The phonon band gap at the Γ-point in π-SnS is reduced at higher pressures, as shown in Fig. 6. This closure is accompanied by a broadening of the spectrum of both sets of modes above and below the band gap, i.e., some modes become harder and some softer with increasing pressure. From an analysis of the change in the
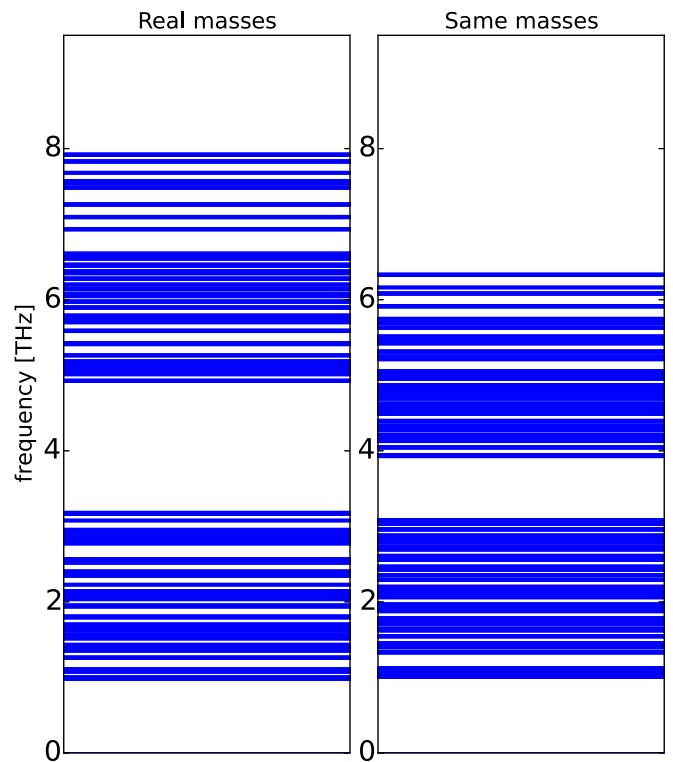

FIG. 5. The Γ-point phonon frequencies in π-SnS. The left panel represents a calculation with the atomic masses set to their physical values, M_{Sn} and M_S. The right panel is a calculation performed with both masses set to an equal value of $(M_{Sn} + M_S)/2$.
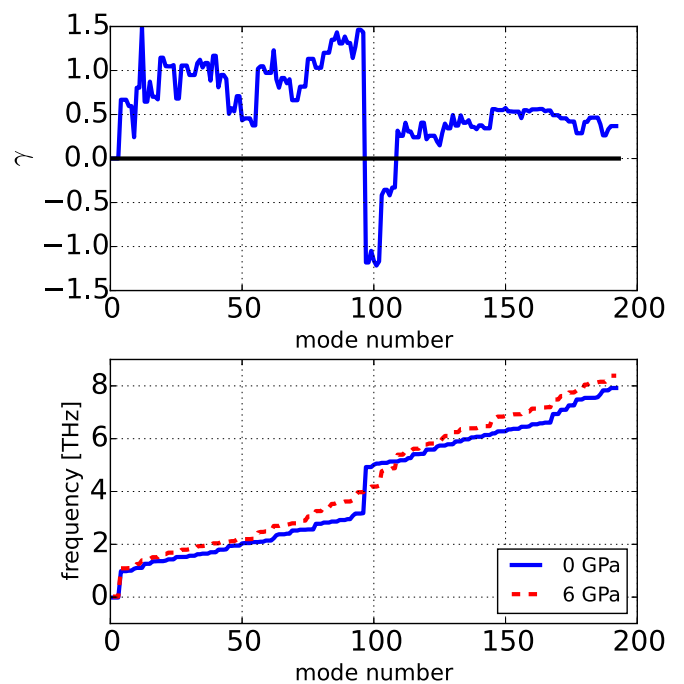

FIG. 6. The mode Grüneisen parameter, γ, calculated using the Γ-point phonon frequencies in π-SnS at 0 and 6 GPa shown in the lower panel.

spectrum between 0 and 6 GPa, we find that the gap closes due to an almost equal shift of phonon states below the gap and states above the gap, see Fig. 6, which indicates that the latter have a negative mode Grüneisen parameter defined as

$$\gamma = -\frac{V}{\omega}\frac{\partial \omega}{\partial V}, \tag{4}$$

where V is the volume and ω is the frequency. However, due to the relatively small number of modes with negative mode Grüneisen parameter values, there is no negative thermal expansion effect in these systems. The closing of the band gap with increasing pressure while the π-phase structure is retained indicates that the phonon band gap is not a purely geometrical property of the structure.

D. Raman spectroscopy: Experimental validation of the phonon band gap in π-SnS and π-SnSe

Raman spectroscopy is used for experimentally measuring the phonon frequencies. To verify the crystal structure of the samples, we have used x-ray diffraction. The results indicate that the samples indeed correspond to the π-SnS and π-SnSe crystal structure (Fig. 7), which ensures the relevance of the Raman measurements to our calculations.

The π-phase SnS and SnSe specimens were cooled down to liquid nitrogen (77 K) temperature and the Raman measurements were carried out. The phonon spectrum of π-SnS shown in Fig. 8(a) ranges from approximately 1.5 to 7 THz (the peak at 8 THz is attributed to SnS$_2$ [45]), and a phonon band gap of ~1.5–2 THz is apparent around the center of the spectrum. For π-SnSe [Fig. 8(b)], the phonon spectrum ranges from approximately 1.2 to 5.4 THz (similarly, the peak centered around 6.2 THz is attributed to SnSe$_2$ [45]) and a phonon band gap of ~1.5–1 THz can be identified around
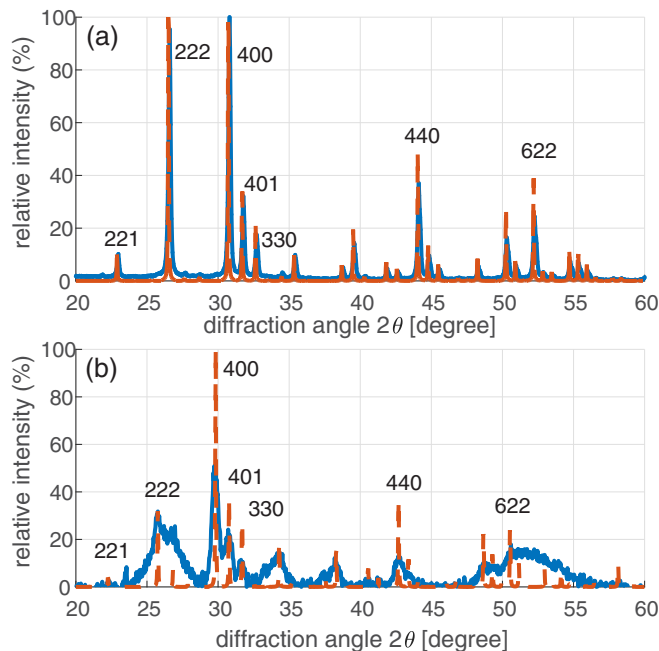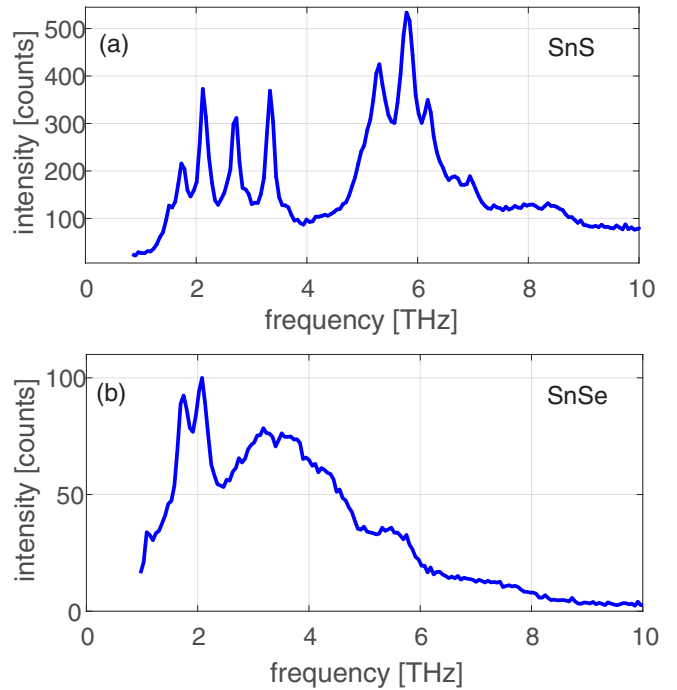
FIG. 8. Raman spectrum of (a) π-SnS and (b) π-SnSe at liquid nitrogen temperature.

the center of the spectrum. These results are in excellent agreement with the theoretical predictions reported above both with respect to the spectrum range and to the band-gap width and location.

One of the differences between the orthorhombic and cubic polymorphs is in the property of centrosymmetry, namely the presence or absence of an inversion center in the crystal. Non-centrosymmetric crystals can be polar, chiral, both, or neither. The absence of an inversion center in the cubic phase makes this phase noncentrosymmetric, and according to the space group ($P2_13$), also chiral. For noncentrosymmetric crystals all Γ-point phonons give rise to Raman active modes. Chirality of a crystal can be accompanied by other useful crystal properties such as enantiomorphism, piezoelectricity, and optical activity [30], which are yet to be studied in these materials.

IV. PHONON BAND-GAP RESULTS

Having established above that the existence of the phonon band gap is not determined uniquely either by the mass differences or by the crystal structure, and that furthermore the characteristics of the modes below and above the band gap are different, we proceed to analyze the two sets of modes by employing the quantitative measures introduced above to elucidate the differences between them.

A. Relative motion of the two atomic types—the effect of different masses

The RMRs of the atoms in π-SnS were calculated for all the phonon modes, both with their real atomic masses, M_{Sn} and M_S, and with a fictitious, equal atomic mass of $M = (M_{Sn} + M_S)/2$, and the results are presented in Fig. 9. Where the atoms have equal masses, the RMR is approximately 1 for

FIG. 7. X-ray diffraction pattern for as-synthesized samples of (a) π-SnS and (b) π-SnSe. Solid lines are the experimental results, and dashed lines are reference patterns [31,44].
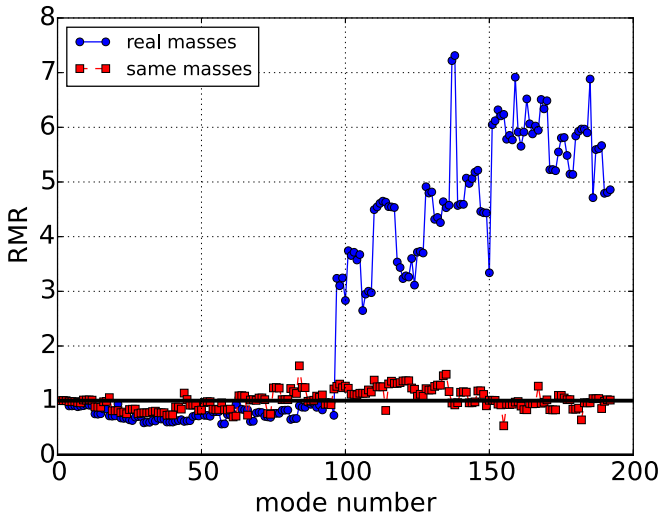
FIG. 9. Relative motion ratio (RMR), as defined in the text, in π-SnS, of S and Sn atoms with real atomic masses and fictitious masses as in Fig. 5.

all the normal modes. However, when the RMR is calculated for the modes with the real atomic masses, we find that it is smaller than 1 for normal modes below the gap and larger than 1 above the gap. This means that in normal modes below the gap, the Sn atoms (heavy atoms) move relatively more and above the gap the S atoms (light atoms) move with a larger relative amplitude.

From this analysis and the results in the previous section, it is clear that mass plays a significant role in enhancing the phonon band gap but does not in itself create it. We surmise that the additional necessary condition for the formation of the band gap in the π-phase is possibly due to the existence of two types of chemical bonds originating in the structural distortion.

B. The deformation/rigidity of the bonds—the effect of structural distortion

In π-SnS, the three-dimensional structure is tetrahedral, resulting from symmetry breaking of the high-symmetry rock-salt phase [26]. The six degenerate bonds to the six nearest neighbors in rocksalt split into three first-nearest-neighbor bonds and three second-nearest-neighbor bonds in the π-phase.

The MDP was calculated for the normal modes of π-SnS, and the results are presented in Fig. 10. At the band gap there is a large discontinuity in the MDP of the modes calculated both with the real masses and with equal masses. The MDP reaches approximately 1 at the high-frequency modes corresponding to almost pure compression of the nearest-neighbor bonds and has a value of less than approximately 0.5 for the low-frequency modes. In contrast to the RMR, the MDP does not change significantly as the masses are varied because the MDP is mainly determined by the bond strengths.

Examples of modes with large and small MDP values are shown in Fig. 11. The mode with a large MDP does not include rigid motion of nearest-neighbor bonds [Fig. 11(a)] together with a large difference between the motion of the
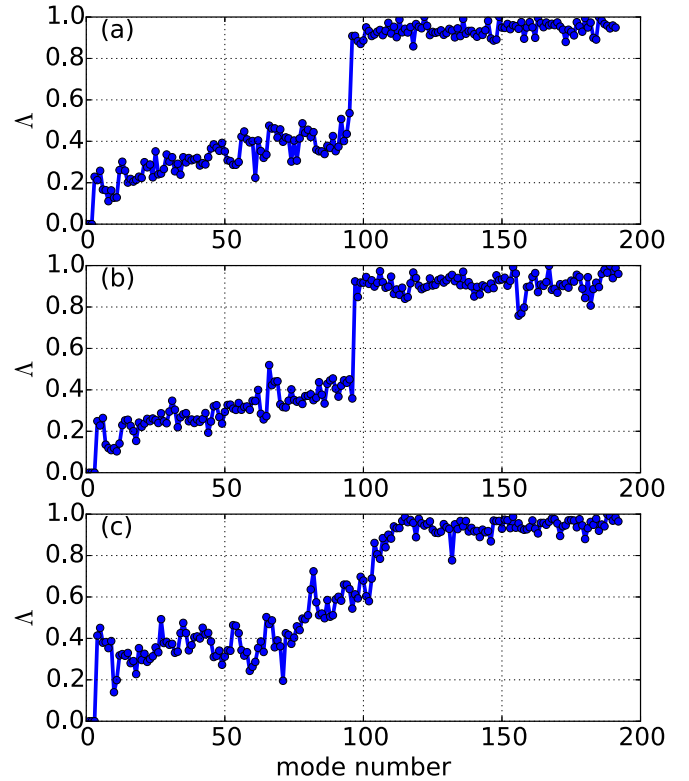

FIG. 10. The mode deformation parameter (MDP) of π-SnS, as defined in the text, Eq. (3), for (a) real masses at zero pressure, (b) equal masses at zero pressure, and (c) real masses at 10 GPa. The modes are ordered from the lowest-frequency mode to the highest-frequency mode.

two different types of atoms (large RMR). In contrast, the mode with a small MDP exhibits rigid motion of groups of nearest-neighbor bonds [Fig. 11(c)].

For π-SnS, at 10 GPa, no discontinuity is present in the MDP [Fig. 10(c)] and there is also no phonon gap. This correspondence indicates that the origin of the phonon gap is not the relative motion, caused by the mass difference, but it is the combination of structure and bonding that affects the rigidity of the modes.

C. The orthorhombic and rhombohedral phases

The phonon spectra of GeSe and GeTe in the rhombohedral phase were calculated and are presented in Figs. 12 and 13. Similar results are obtained for both materials. At zero pressure, there is no phonon band gap. At negative pressure, a gap opens. This is the result of the larger distortion at negative pressure. The distortion parameters are α, the angle between the primitive lattice vectors, and τ, which is the displacement between the two atoms from their high-symmetry rocksalt positions [28]. For GeSe, these parameters change from $\alpha = 58°$, $\tau = 0.027$ at 2 GPa to $\alpha = 54°$, $\tau = 0.047$ at -2 GPa (τ is in units of the lattice parameter) [28]. In this case, the modes below the band gap are acoustic and the modes above are optical.

The phonon spectrum was calculated for the orthorhombic phase of SnS, which has an eight-atom primitive unit cell. A small phonon band gap appears in its spectrum, as
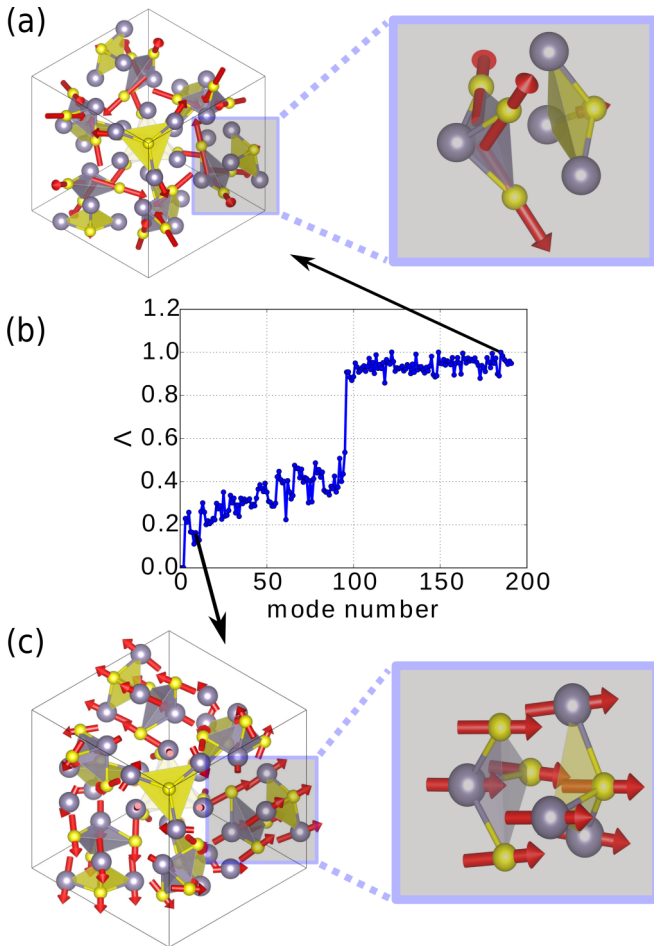
FIG. 13. Phonon density of states of GeTe in the rhombohedral phase at -2, 0, and 2 GPa.

can be seen in Fig. 14. The MDP was calculated for all modes at the Γ point and is found to be larger for the modes above the gap than the modes below the gap and reaching 1 for the highest-frequency modes (Fig. 14). The

FIG. 11. Two normal modes for π-SnS: (a) high-frequency mode with large MDP, number 185, (b) the MDP, and (c) low-frequency mode with low MDP, number 9. The gray and yellow spheres represent tin and sulfur atoms, respectively. These two modes have a C3 rotation symmetry around the [111] axis, and the viewing direction is [111].
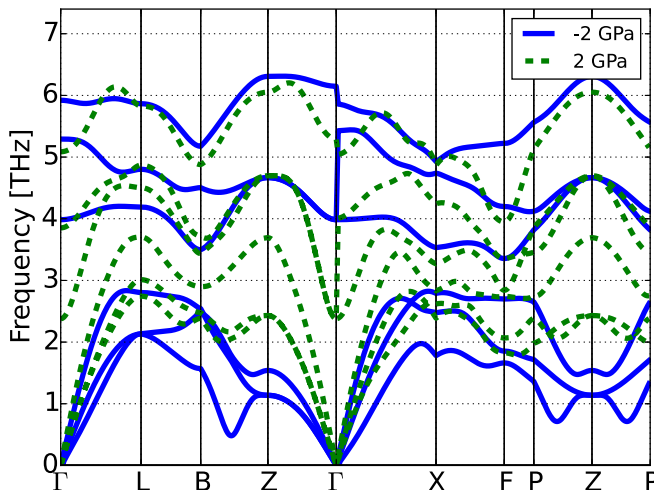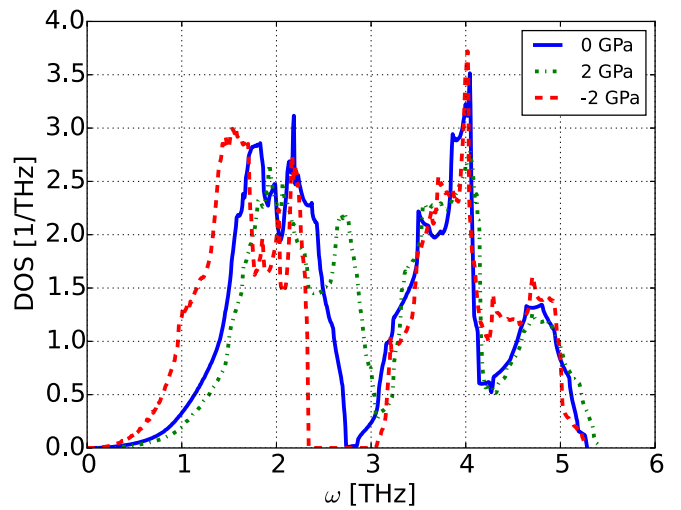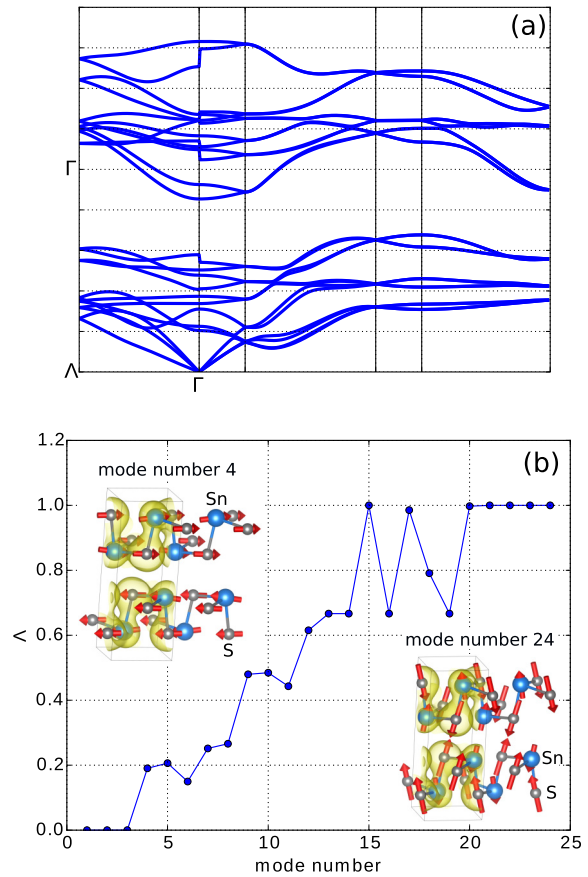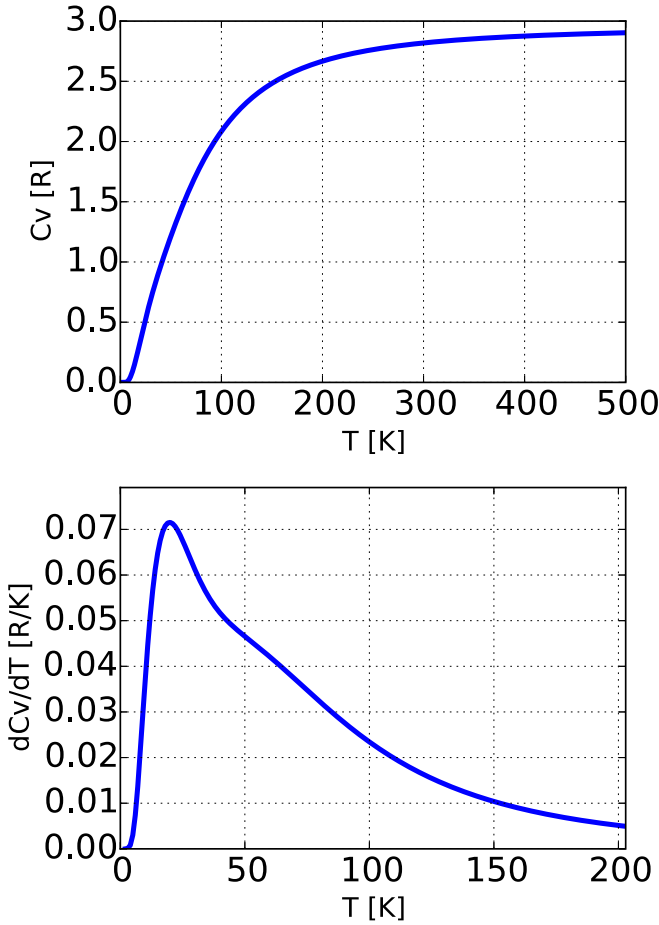

FIG. 14. (a) The phonon spectrum of the orthorhombic phase of SnS and (b) the MDP calculated from the Γ-point modes. The insets in (b) are a visualization of two modes (in mode 24 the Sn magnitude of the Sn vector arrows is three times larger for visualization purposes). Low-density isosurfaces of 17% of the maximum density value also shown in the unit cell in the insets to indicate the bonding.

FIG. 12. Phonon spectrum of GeSe in the rhombohedral phase at -2 and 2 GPa.

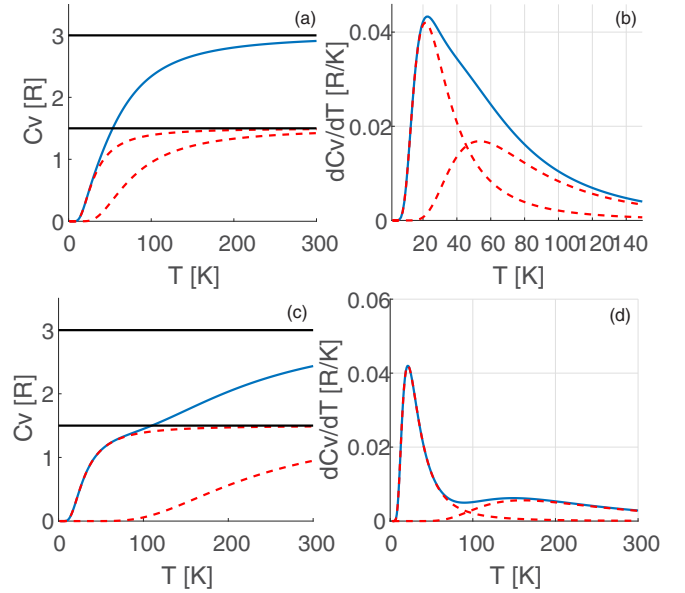FIG. 15. Heat capacity and its temperature derivative in π-SnS.

FIG. 16. Molar heat capacity [(a) and (c)] and its temperature derivative [(b) and (d)] of two Einstein models with frequencies of 2 and 5 THz for (a) and (b), and 2 and 15 THz for (c) and (d). The black solid lines in (a) and (c) simply indicate the values of 3/2 and 3. The red dashed lines are the contributions of each Einstein mode separately, and the blue solid lines are the combined contributions.

lowest-frequency mode (the lowest nonzero frequency mode at the Γ-point), mode number 4, is shown in the inset of Fig. 14(b). This mode is a motion of almost the entire layer moving together, which makes its MDP value small, approximately 0.2. In contrast, the highest-frequency mode, number 24, also illustrated in Fig. 14, exhibits nonparallel motions of the neighboring atoms. This leads to the MDP having its maximal value reflecting compression of all the bonds in this mode. A low-density isosurface is also shown in these insets, indicating the nearest-neighbor bonds.

D. Thermodynamic heat capacity

The heat capacity of π-SnS and its temperature derivative were calculated in the harmonic approximation from the phonon frequencies by the expression

$$Cv = \sum_{i} \frac{\partial}{\partial T} \left(\frac{\hbar\omega_i}{e^{\hbar\omega_i/(k_B T)} - 1} \right)_V \tag{5}$$

and the results are presented in Fig. 15. A small anomaly is observed in the temperature derivative around 40 K, which originates from the phonon band gap.

To study the possible effect of the phonon band gap on the heat capacity, we constructed a model consisting of two Einstein frequencies representing the modes below and above the phonon band gap (Fig. 16). We assume that the

three acoustic modes that exhibit a Debye behavior will only make a significant contribution to the specific heat at low temperatures due to the large number of optical modes. In this two-frequency model, an equal number of modes is associated with each frequency, representing an equal number of modes below the band gap and above it, as is the situation in the π-phase.

A low-temperature anomaly is present in the heat capacity of this model, and is apparent in its temperature derivative. The anomaly increases with the magnitude of the frequency difference (band gap) between the two Einstein frequencies. If the difference is approximately 3 THz, of the order of magnitude calculated for the π-phase structures, the anomaly is barely distinguishable. As the band gap is increased to 13 THz, the anomaly becomes more significant. From these results, we expect the band gap in π-SnS to be too small to have a significant effect on the heat capacity, as is indeed found from the calculated heat capacity for π-SnS. Only materials with a larger band gap will exhibit a significant effect.

V. DISCUSSION

A. π-phase phonons

The phonon spectra of all four proposed π-phase material systems have been calculated and they are all found to exhibit a large phonon band gap in the optical phonon spectrum. For π-SnS our results agree well with the earlier work of Skelton *et al.* [27]. The calculated positive frequencies of π-GeS and π-GeSe (Fig. 4) suggest that these phases are at least metastable, and in an earlier study we showed that they are energetically competitive with the experimentally stable phases

in these materials [26]. To date, the experimental search for synthesizing of the GeS or GeSe π structure continues.

An analysis of the polarization reveals two characteristics of the phonon modes about the band gap: A difference in the relative motion and a difference in the rigidity of the modes. The structural distortion creates the differences in the rigidity between the modes below and above the band gap and thus forms the band gap (Fig. 3). The mass difference increases the band gap by affecting the relative motion of the two types of atoms without reducing the differences in the rigidity [see Figs. 11(a) and 10].

B. Band gap in the monochalcogenides and structural distortion

All the common phases of the IV-VI monochalcogenides have a tetrahedral structure in which all atoms have three nearest neighbors and that can be thought of as a distorted rock-salt. The six nearest neighbors of the rocksalt phase split into three first nearest neighbors and three second nearest neighbors. The symmetry is broken differently in each phase, as reflected by the geometrical arrangement of the tetrahedra with respect to each other. The strong impact of rearranging bonds on the phonon spectrum can be seen in the case of the high-temperature phase transition from the orthorhombic *Pnma* structure to the more symmetric *Cmcm* structure, which does not exhibit a phonon band gap [46] and is illustrated in a simple two-dimensional model (see Appendix B). All the atoms have the same number of strong bonds and the same number of weak bonds with different geometries, which is similar to the situation in the phases of the IV-VI monochalcogenides. Every phase has the same number of first nearest neighbors and second nearest neighbors (except rocksalt) and an entirely different phonon spectrum.

C. Thermoelectric properties

Thermoelectric properties are characterized by a figure of merit defined as

$$ZT = \frac{\sigma S^2}{k} T, \qquad (6)$$

where σ is the electrical conductivity, S is the Seebeck coefficient, k is the thermal conductivity, and T is the temperature. For good thermoelectric materials, ZT should be large. Thus, the thermal conductivity should be as low as possible. Ultrahigh ZT is found for SnSe single crystals along one of the directions and has been attributed to the high anharmonicity [22]. A phonon band gap can lead to high thermal conductivity because some phonon-phonon scattering processes, two acoustic phonons to one optical phonon, become inefficient [10,14,15]. Thus, materials with a phonon band gap are probably less suitable for thermoelectric applications.

VI. CONCLUSIONS

Phonon band gaps were found in a variety of monochalcogenide phases, with different magnitudes, and they were analyzed in terms of the relative motion of the two atomic species and the rigidity of the bonds. In particular, the newly discovered π-phase is found to be mechanically stable in all the materials considered. In π-SnS and π-SnSe, Raman

measurements confirm the existence and magnitudes of the calculated phonon band gaps. The normal modes below and above the gap are found to have significantly different relative motion and rigidity. These differences in the properties are primarily due to the existence of two types of bonds with different bond strengths, and this is the origin of the phonon band gap. The mass differences between the atoms merely enhance these effects. These conclusions improve our understanding of phonon band-gap formation in real three-dimensional crystals and thus lay the foundation for future phonon band-gap engineering.

APPENDIX A: THE DEFORMATION OF BONDS

The bond deformation parameter is defined to characterize the deformation or rigidity of bonds in a phonon normal mode. It is common knowledge that the rigidity/deformation of phonon normal modes is related to the frequency. For example, the acoustic modes at the Γ point have zero frequency because the displacement of the atoms is fully rigid. To obtain a quantitative measure for the rigidity/deformation, we will use a similar definition to the macroscopic strain, which is exactly zero for rigid translations or rotations.

Let us define the x-axis on the direction of the bond with the origin on one of the atoms of the bond. Using just rigid translation, we can always move one of the atoms after the phonon displacements back to the origin. Both bonds, before and after the phonon displacements, are on one plane. The strain in the direction of the bond, ϵ_{xx}, is [47]

$$\epsilon_{xx} = \frac{\partial u_x}{\partial x} + \frac{1}{2}\left[\left(\frac{\partial u_x}{\partial x}\right)^2 + \left(\frac{\partial u_y}{\partial x}\right)^2\right], \qquad (A1)$$

where u_x and u_y are the displacements in the x and y direction, respectively. Let L be the bond distance before the displacement and L' the bond distance after the displacement with magnitude ϵ:

$$L = |\vec{R}_1 - \vec{R}_2|, \qquad (A2)$$

$$L'(\epsilon) = |\vec{R}_1 + \vec{P}_1 \cdot \epsilon - (\vec{R}_2 + \vec{P}_2 \cdot \epsilon)|, \qquad (A3)$$

where $\vec{R}_1$, $\vec{R}_2$, $\vec{P}_1$, and $\vec{P}_2$ are the position of atom 1, the position of atom 2, the polarization of atom 1, and the polarization of atom 2, respectively. We further assume that the deformation is homogeneous. Using these definitions, the strain becomes

$$\epsilon_{xx} = \frac{1}{2}\left[\left(\frac{L'(\epsilon)}{L}\right)^2 - 1\right]. \qquad (A4)$$

Because we want to describe a bond under a deformation in a phonon mode, the deformation/rigidity should be characterized independently of the amplitudes (without dependence on the temperature). Requiring the parameter to be dimensionless with values between 0 and 1, we introduce the following definition, based on Eq. (A4):

$$\Delta = \lim_{\epsilon \to 0} \frac{L \cdot |\epsilon_{xx}|}{|\vec{P}_1 \cdot \hat{r}_{12} \cdot \epsilon| + |\vec{P}_2 \cdot \hat{r}_{12} \cdot \epsilon|}. \quad (A5)$$

Substitution of ϵ_{xx} gives

$$\Delta = \lim_{\epsilon \to 0} \frac{\frac{L}{2}\left[\left|\left(\frac{L'(\epsilon)}{L}\right)^2 - 1\right|\right]}{|\vec{P}_1 \cdot \hat{r}_{12} \cdot \epsilon| + |\vec{P}_2 \cdot \hat{r}_{12} \cdot \epsilon|}. \quad (A6)$$

Substituting for $L'(\epsilon)$ yields

$$\Delta = \lim_{\epsilon \to 0} \frac{\frac{L}{2}\left(\left|\frac{\sum_i [R_1^i + P_1^i \cdot \epsilon - (R_2^i + P_2^i \cdot \epsilon)]^2}{L^2} - 1\right|\right)}{|\vec{P}_1 \cdot \hat{r}_{12} \cdot \epsilon| + |\vec{P}_2 \cdot \hat{r}_{12} \cdot \epsilon|}, \quad (A7)$$

where the sum is over the Cartesian coordinates. After some calculations, the final form is

$$\Delta = \frac{|(\vec{P}_1 - \vec{P}_2) \cdot \hat{r}_{12}|}{|\vec{P}_1 \cdot \hat{r}_{12}| + |\vec{P}_2 \cdot \hat{r}_{12}|}. \quad (A8)$$

The bond deformation parameter, Δ, takes values between 0 and 1 and does not depend on the magnitude of the polarization vector. $\Delta = 0$ is a fully rigid motion and $\Delta = 1$ is purely compressive.

APPENDIX B: STRUCTURAL DISTORTION IN TWO-DIMENSIONAL ANALYTICAL ANALYSIS

In materials, the chemical composition determines the number of strong bonds (first nearest neighbors) and weak bonds (second nearest neighbors), but there may also exist several possibilities for the geometrical arrangement of the atoms. The following model is an example where we consider such different arrangements.

To examine the features of the phonon spectrum and especially to identify the origins of the phonon band gap, a simple analytical model is introduced. The model is a two-dimensional lattice, where the atoms are represented as point masses and the chemical bonds are modeled as springs. We use two different spring constants and two cases of the masses: (i) two different masses, m_1 and m_2, and (ii) all atoms have
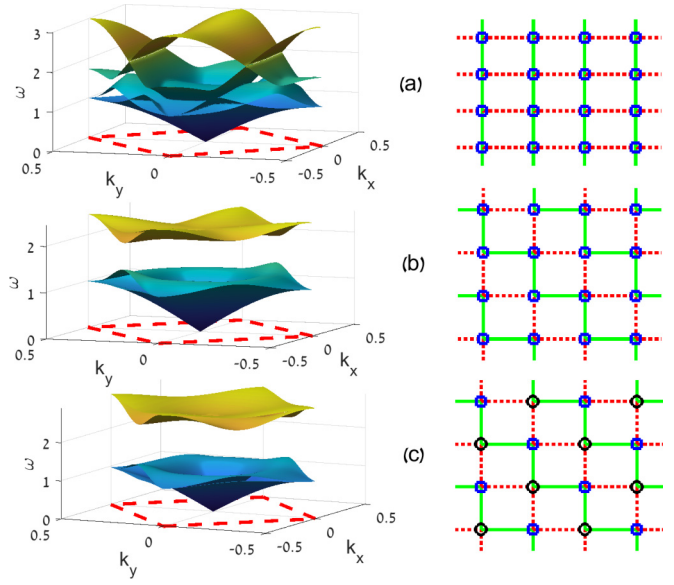

FIG. 17. The calculated phonon spectrum of two-dimensional crystal with two types of bonds noted in the figure as green solid lines and red dashed lines and a bond to the second nearest neighbor (not marked in the figure). Parts (a) and (b) are lattices with one mass, and (c) describes a lattice with two different masses. The red dashed lines in the left panels are the boundaries of the Brillouin zone.

equal average masses of $m = (m_1 + m_2)/2$. This system is a model for real systems with strong bonds to some neighboring atoms and weaker bonds to others, and its configurations are illustrated in Fig. 17.

The dispersion relations of this two-dimensional crystal were calculated analytically and are shown in Fig. 17. In Fig. 17(a) the crystal is a monatomic crystal and thus only acoustic branches occur. These branches are continuous and no phonon band gap can form. A crystal with the same number of strong and weak bonds as in Fig. 17(a) is illustrated in Fig. 17(b), but these bonds now have a different geometrical arrangement and the unit cell contains two atoms. It can be seen in the spectrum that in this geometrical arrangement (or crystal phase), a phonon band gap appears in the spectrum. A further increase in this band gap occurs with different masses for two type of atoms [Fig. 17(c)]. We note that the main changes in the phonon spectrum due to the mass difference are in the branches above the band gap.

[1] D. D. Dlott, Annu. Rev. Phys. Chem. **37**, 157 (1986).

[2] M. T. Dove and H. Fang, Rep. Prog. Phys. **79**, 066503 (2016).

[3] A. K. A. Pryde, K. D. Hammonds, M. T. Dove, V. Heine, J. D. Gale, and M. C. Warren, J. Phys.: Condens. Matter **8**, 10973 (1996).

[4] A. E. Phillips, Acta Crystallogr. Sect. A **74**, 406 (2018).

[5] B. Campbell, C. J. Howard, T. B. Averett, T. A. Whittle, S. Schmid, S. Machlus, C. Yost, and H. T. Stokes, Acta Crystallogr. Sect. A **74**, 408 (2018).

[6] A. P. Giddy, M. T. Dove, G. S. Pawley, and V. Heine, Acta Cryst. **A49**, 697 (1993).

[7] L. Z. Khadeeva and S. V. Dmitriev, Phys. Rev. B **81**, 214306 (2010).

[8] A. A. Kistanov and S. V. Dmitriev, Phys. Solid State **54**, 1648 (2012).

[9] M. Kempa, P. Ondrejkovic, P. Bourges, J. Ollivier, S. Rols, J. Kulda, S. Margueron, and J. Hlinka, J. Phys.: Condens. Matter **25**, 055403 (2013).

[10] L. Lindsay, D. A. Broido, and T. L. Reinecke, Phys. Rev. Lett. **111**, 025901 (2013).

[11] L. Lindsay, D. A. Broido, and T. L. Reinecke, Phys. Rev. B **87**, 165201 (2013).

[12] X. Gu and R. Yang, Appl. Phys. Lett. **105**, 131903 (2014).

[13] X. Gu, Y. Wei, X. Yin, B. Li, and R. Yang, Rev. Mod. Phys. **90**, 041002 (2018).

[14] J. S. Kang, M. Li, H. Wu, H. Nguyen, and Y. Hu, Science **361**, 575 (2018).

[15] Z. Tian, K. Esfarjani, J. Shiomi, A. S. Henry, and G. Chen, Appl. Phys. Lett. **99**, 053122 (2011).

[16] A. Ward and D. A. Broido, Phys. Rev. B **81**, 085205 (2010).

[17] R. E. Peierls, *Quantum Theory of Solids* (Oxford University Press, Oxford, 1955), p. 23.

[18] U. D. Wdowik, K. Parlinski, S. Rols, and T. Chatterji, Phys. Rev. B **89**, 224306 (2014).

[19] S. Shang, Y. Wang, H. Zhang, and Z.-K. Liu, Phys. Rev. B **76**, 052301 (2007).

[20] J.-P. Gaspard, C. R. Phys. **17**, 389 (2016).

[21] N. W. Ashcroft and N. D. Mermin, *Solid State Physics* (Cornell University Press, Ithaca, NY, 1976).

[22] L.-D. Zhao, S.-H. Lo, Y. Zhang, H. Sun, G. Tan, C. Uher, C. Wolverton, V. P. Dravid, and M. G. Kanatzidis, Nature (London) **508**, 373 (2014).

[23] R. E. Abutbul, E. Segev, U. Argaman, G. Makov, and Y. Golan, Adv. Mater. **30**, 1706285 (2018).

[24] A. Rabkin, S. Samuha, R. E. Abutbul, V. Ezersky, L. Meshi, and Y. Golan, Nano Lett. **15**, 2174 (2015).

[25] S. Lin, A. Carvalho, S. Yan, R. Li, S. Kim, A. Rodin, L. Carvalho, E. M. Chan, X. Wang, A. H. C. Neto *et al.*, Nat. Commun. **9**, 1455 (2018).

[26] E. Segev, U. Argaman, R. E. Abutbul, Y. Golan, and G. Makov, Cryst. Eng. Commun. **19**, 1751 (2017).

[27] J. M. Skelton, L. A. Burton, F. Oba, and A. Walsh, APL Mater. **5**, 036101 (2017).

[28] U. Argaman, R. E. Abutbul, E. Segev, and G. Makov, Cryst. Eng. Commun. **19**, 6107 (2017).

[29] Y. Zhang, X. Ke, C. Chen, J. Yang, and P. R. C. Kent, Phys. Rev. B **80**, 024304 (2009).

[30] R. E. Abutbul, A. R. Garcia-Angelmo, Z. Burshtein, M. T. S. Nair, P. K. Nair, and Y. Golan, Cryst. Eng. Commun. **18**, 5188 (2016).

[31] R. E. Abutbul, E. Segev, L. Zeiri, V. Ezersky, G. Makov, and Y. Golan, RSC Adv. **6**, 5848 (2016).

[32] E. Barrios-Salgado, L. A. Rodríguez-Guadarrama, M. L. R. García, L. G. Martínez, M. T. S. Nair, and P. K. Nair, Phys. Status Solidi A **214**, 1700036 (2017).

[33] P. K. Nair, A. R. Garcia-Angelmo, and M. T. S. Nair, Phys. Status Solidi A **213**, 170 (2015).

[34] S. ur Rehman, F. K. Butt, Z. Tariq, F. Hayat, R. Gilani, and F. Aleem, J. Alloys Compd. **695**, 194 (2017).

[35] J. M. Skelton, L. A. Burton, A. J. Jackson, F. Oba, S. C. Parker, and A. Walsh, Phys. Chem. Chem. Phys. **19**, 12452 (2017).

[36] V. L. Deringer, R. P. Stoffel, and R. Dronskowski, Phys. Rev. B **89**, 094303 (2014).

[37] S. Baroni, S. de Gironcoli, A. Dal Corso, and P. Giannozzi, Rev. Mod. Phys. **73**, 515 (2001).

[38] S. Baroni, P. Giannozzi, and E. Isaev, Rev. Mineral. Geochem. **71**, 39 (2010).

[39] S. de Gironcoli, Phys. Rev. B **51**, 6773 (1995).

[40] R. M. Martin, *Electronic Structure: Basic Theory and Practical Methods* (Cambridge University Press, Cambridge, 2008).

[41] P. Giannozzi, S. Baroni, N. Bonini, M. Calandra, R. Car, C. Cavazzoni, D. Ceresoli, G. L. Chiarotti, M. Cococcioni, I. Dabo *et al.*, J. Phys.: Condens. Matter **21**, 395502 (2009).

[42] J. P. Perdew, K. Burke, and M. Ernzerhof, Phys. Rev. Lett. **77**, 3865 (1996).

[43] A. Walsh and G. W. Watson, J. Phys. Chem. B **109**, 18868 (2005).

[44] R. E. Abutbul, E. Segev, S. Samuha, L. Zeiri, V. Ezersky, G. Makov, and Y. Golan, Cryst. Eng. Commun. **18**, 1918 (2016).

[45] D. Mead and J. Irwin, Solid State Commun. **20**, 885 (1976).

[46] J. M. Skelton, L. A. Burton, S. C. Parker, A. Walsh, C.-E. Kim, A. Soon, J. Buckeridge, A. A. Sokol, C. R. A. Catlow, A. Togo, and I. Tanaka, Phys. Rev. Lett. **117**, 075502 (2016).

[47] L. D. Landau and E. Lifshitz, *Theory of Elasticity* (Elsevier, New York, 1986), Vol. 7.